Downloaded from UvA-DARE, the institutional repository of the University of Amsterdam (UvA)
http://dare.uva.nl/document/122465

File ID	122465
Filename	2: Theoretical background
Version	Final published version (publisher's pdf)

SOURCE (OR PART OF THE FOLLOWING SOURCE):

Type	Dissertation
Title	Bose-Einstein condensates in radio-frequency-dressed potentials on an atom chip
Author	J.J.P. van Es
Faculty	Faculty of Science
Year	2009
Pages	VIII, 131
ISBN	978-90-5776-186-7

FULL BIBLIOGRAPHIC DETAILS:
http://dare.uva.nl/record/292198

Copyright

It is not permitted to download or to forward/distribute the text or part of it without the consent of the author(s) and/or copyright holder(s), other then for strictly personal, individual use.

UvA-DARE is a service provided by the library of the University of Amsterdam (http://dare.uva.nl)

2 Theoretical background

2.1 Introduction

This chapter provides some theoretical background to the subsequent experimental chapters. The main focus is on the magnetic potentials, both static and rf-dressed, in which we trap and manipulate ultra cold atoms.

This chapter is organized as follows. In Sec. 2.2.1 we present the basic principles behind magnetic trapping and expressions for the field of the Ioffe-Pritchard trap. In Sec. 2.2.2 we discuss the scaling laws that govern the magnetic field gradient in microtraps and show why the use of microtraps is favorable. We present our specific microtrap geometry: an atom chip structure with two separate wires. Sec. 2.2.3 contains expressions for several approximations to the static magnetic field generated by the atom chip. We continue in Sec. 2.3 by characterizing the rf-dressed potential that comes about when a radio-frequency magnetic field is added to the static field. The expression for the potential is presented in Sec. 2.3.1 after a brief description of the derivation. A detailed derivation is contained in Appendix A. We describe the way we generate the rf field on our chip and present expressions for the rf field strength in Sec. 2.3.2. Section 2.3.3 describes the transverse shape of the rf-dressed potential ranging from single well, double-well to Mexican hat. We discuss the influence of electrostatic fields on the trapped atoms in Sec. 2.4 and conclude the chapter with a description of the in-trap density distribution for both a (quasi-)BEC and a thermal cloud (Sec. 2.5).

2.2 Magnetic trapping

2.2.1 Basic principles

The idea of magnetic trapping [89] is that in a magnetic field $\mathbf{B}$, a neutral atom with a magnetic moment $\boldsymbol{\mu}$ will have quantum states whose Zeeman energy increases with increasing field and states whose energy decreases, depending on the orientation of the magnetic moment compared to the field. The increasing-energy states, called *low-field seekers*, can be trapped in a region where the magnitude of the magnetic field has a minimum. The decreasing-energy states, called *strong-field seekers* cannot be trapped because it is impossible to create a static magnetic field maximum in

free space. For a proof, see Wing's theorem [90] which is specifically about magnetic fields while the similar Earnshaw theorem [91] only deals with electrostatic fields (see also [92] and [93]).

In this thesis, we restrict ourselves to relatively modest magnetic fields, where the Zeeman shift is linear in $|\mathbf{B}|$ and the magnetic interaction energy can be written as

$$U_{\text{mag}} = -\boldsymbol{\mu} \cdot \mathbf{B} = m_F g_F \mu_B |\mathbf{B}|, \tag{2.1}$$

where m_F is the magnetic quantum number of the atomic state (with angular momentum F), $m_F = -F, \ldots, F$, g_F is the Landé factor and μ_B the Bohr magneton. Low-field seekers have $g_F m_F > 0$ while the strong-field seekers have $g_F m_F < 0$. Of course the $m_F = 0$ state can also not be trapped magnetically since its potential is independent of the magnetic field. In all our experiments we work with ^{87}Rb that in the electronic ground state has either $F = 1$ or $F = 2$. We use $F = 2$.

For stable trapping it is necessary that the kinetic energy of the atom is lower than the depth of the magnetic potential well, and that the magnetic moment must move adiabatically in the magnetic field. The latter condition means that the changes in $\mathbf{B}$ (due to movement of the atom through the field) must be slow, such that the orientation of the magnetic moment can follow and stay unchanged with respect to the field. This adiabaticity condition can be expressed as

$$\frac{d\omega_L}{dt} \ll \omega_L^2, \tag{2.2}$$

with the Larmor frequency, ω_L, the frequency at which the magnetic moment precesses about the magnetic field direction, (corresponding to the Zeeman-level spacing), given by

$$\omega_L = \frac{g_F \mu_B}{\hbar} |\mathbf{B}|. \tag{2.3}$$

The adiabaticity condition is violated in regions where the magnetic field is too small. In such a region the spin cannot follow the changing direction of the magnetic field and might flip its orientation relative to the field, changing m_F in Eq. (2.1). A spin flip like this is named after the Italian physicist Majorana and the associated loss of atoms from a magnetic trap is known as Majorana losses [94]. Sukumar and Brink have studied Majorana spin flips in detail [95]. It is the task of the experimentalist to construct his magnetic trap such that even in the magnetic field minimum the field is sufficiently large to prevent losses.

Ioffe-Pritchard trap

The standard magnetic-field configuration used nowadays for magnetostatic trapping of ultracold gases has a non-zero minimum field, and is known as the Ioffe-Pritchard trap [39,40]. Near the minimum of the potential, the field can be expressed in cylindrical coordinates (r, ϕ, z) as [89, 96]

$$\begin{aligned} B_r &= -Gr \sin 2\phi - Crz, \\ B_\phi &= -Gr \cos 2\phi, \\ B_z &= B_0 + Cz^2 - \tfrac{1}{2}Cr^2, \end{aligned} \tag{2.4}$$

where G is the transverse field gradient and C the curvature of the longitudinal field. Note that the field is realistic in the sense that it is divergence- and curl-free, satisfying the two relevant Maxwell equations

$$\boldsymbol{\nabla} \cdot \mathbf{B} = 0, \tag{2.5}$$

$$\boldsymbol{\nabla} \times \mathbf{B} = \mathbf{0}. \tag{2.6}$$

Close to the field minimum, the field strength $B = |\mathbf{B}|$ may be expanded yielding

$$B = B_0 + Cz^2 + \frac{1}{2}\left(\frac{G^2}{B_0} - C\right) r^2, \tag{2.7}$$

which is rotationally symmetric.

This expression is based on the conventional configuration in which the longitudinal confinement is generated by coils positioned such that their axes coincide with the axis of the trap. Although useful as a first approximation for chip-based Ioffe-Pritchard traps, the expression is often not sufficient, because of the close proximity and non-symmetric positioning of the field-producing currents on atom chips. In the following we will present a number of useful expressions for the magnetic field generated by atom chips based on current-carrying wires.

2.2.2 Atom-chip magnetic traps

The standard way to calculate the magnetic field of a current-carrying structure is to integrate the Biot-Savart law [97], i.e.,

$$d\mathbf{B} = \frac{\mu_0 I}{4\pi} \frac{d\mathbf{l} \times \mathbf{r}}{r^3}, \tag{2.8}$$

where $d\mathbf{B}$ is the magnetic field generated by a piece of wire $d\mathbf{l}$, I is the current in the wire, μ_0 the permittivity of free space, $\mathbf{r}$ the position vector connecting $d\mathbf{l}$ and $d\mathbf{B}$, and $r = |\mathbf{r}|$.

For instance, by integrating the Biot-Savart law [Eq. (2.8)] in one direction we find the well-known result of the magnetic field of an infinitely long, thin, straight wire through which a current I runs. In cylindrical coordinates the only non-zero component is

$$B_\phi = \frac{\mu_0 I}{2\pi r}, \tag{2.9}$$

where the radial coordinate r is the distance from the wire. In fact, this result is also valid for a cylindrical wire with radius R, as long as $r > R$. The gradient in magnetic field strength is

$$\frac{\partial |\mathbf{B}|}{\partial r} = -\frac{\mu_0 I}{2\pi r^2}. \tag{2.10}$$

The latter result can be used to illustrate the power of microfabricated atom chips over other (cm-sized) traps based on current-carrying wires. Consider the magnetic field at the distance $r \geq R$ from an infinitely long cylindrical wire with radius R.

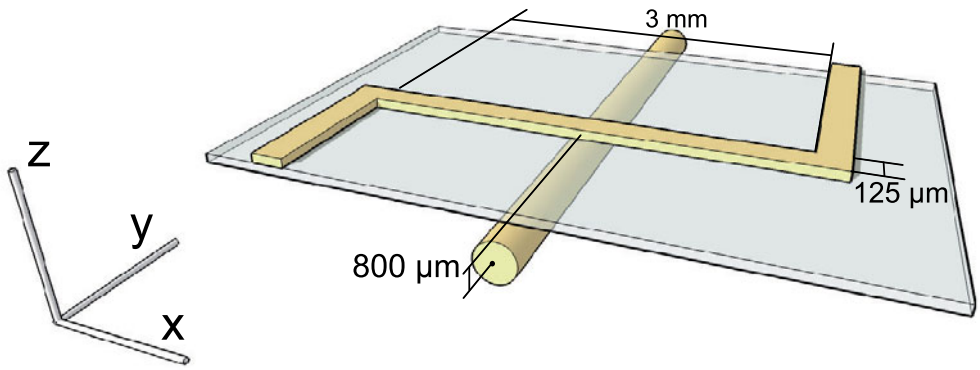

Figure 2.1: Geometry of the two most important field-generating wires in our magnetic trap. Dimensions of the wires are not to scale. The upper wire has a rectangular cross section and lies on a substrate. It has a Z-like shape. The wire underneath the substrate has a circular cross section. The coordinate system is also indicated.

Decreasing the wire radius decreases the minimum r. Reducing r from cm-scale to μm-scale increases the magnetic field gradient by orders of magnitude, allowing for much tighter traps, in which in it possible to perform rapid evaporative cooling because the collision rate is so much larger. In reality the scaling is often somewhat less favorable than suggested by Eq. (2.10), because the allowed current also depends on r [49, 88, 98]. For instance, when heat removal is the limiting factor, the following scaling is relevant: The generated power in the wire per unit length P_{gen} is proportional to I^2/R^2. The power has to be removed via the outside area of the wire, thus the removed power per unit length P_{rem} is proportional to R. Equating P_{gen} and P_{rem} yields $I_{\text{max}} \propto R^{3/2}$, so that the maximum achievable gradient scales as $R^{-1/2}$, showing it is still favorable to reduce the wire diameter [99].

Wire geometry

A sketch of the geometry of two key wires in our atom chip assembly is shown in Fig. 2.1 together with the coordinate system used. These two wires are closest to the ultracold atoms in our static magnetic trap. In order to accurately describe the magnetic trapping potential, we will need accurate expressions for the magnetic fields they generate. The wire on top has the shape of a Z. It is part of the atom chip that was made using micro-fabrication techniques (see Ch. 3). It lies on a flat substrate and has a rectangular cross section and the central part has a length L. The two ends of the chip wire are perpendicular to the central section. Such Z-shaped wires are commonly used on atom chips [49, 51], because (as we will see), when combined with a homogeneous external field they generate a robust and strongly confining IP trap, trapping the atoms at the center of the central section.

Intuitively it is easy to see why the Z-shaped wire gives a three-dimensional trap. The central section, together with an external bias field in the y direction, provides confinement in the y-z plane of Fig. 2.1, resulting in a waveguide along x. The field

of the waveguide, together with a uniform field in the x direction, B_I, is conveniently described by

$$\mathbf{B} = \begin{pmatrix} B_I \\ Gz \\ Gy \end{pmatrix}, \tag{2.11}$$

where G the local field gradient of the wire and B_I is the 'Ioffe' field, the field in the direction of x that offsets the magnetic field minimum from zero. The expression for the absolute field strength

$$|\mathbf{B}| = \sqrt{B_I^2 + G^2\left(y^2 + z^2\right)}, \tag{2.12}$$

clearly shows the confinement in the y-z plane and the lack of confinement in the x direction.

The two ends of the Z contribute to the longitudinal bias field, with the largest contribution directly over the wire ends. As a consequence the middle of the central section has lower longitudinal field, providing confinement longitudinally.

The second wire we call the miniwire. It lies underneath the substrate, has a circular cross section and runs parallel to the two ends of the chip wire. The miniwire generates an additional spatially varying field in the longitudinal direction and allows to tune the longitudinal confinement of the Z trap. The exact details of the trapping field will be calculated in the following sections.

We are interested in the field above the central part of the chip wire as this is the place where we will trap and manipulate cold atoms. Thus the precise details of the current paths in the wires beyond the edges of the sketch in Fig. 2.1 will be ignored for now. The details of the wire ends do not substantially change the field geometry near the atoms because these wire segments are so much further removed from the atoms [cf. Biot Savarts law, Eq. (2.8)]. In order to obtain analytical expressions we will assume that the wire ends extending beyond the edges of Fig. 2.1 continue straight to infinity.

2.2.3 Realistic trapping fields

This section is devoted to finding realistic descriptions of the static trapping fields of the two wires in Fig. 2.1. We will derive a useful expression by going from the simple thin wire formula to increasingly complicated expressions. We start with the miniwire, and take it to be aligned along y, infinitely long, and at a depth d below the chip surface. Expressing Eq. (2.9) in Cartesian coordinates yields

$$\mathbf{B}(x,y,z) = \frac{\mu_0 I}{2\pi\left(x^2 + (z+d)^2\right)} \begin{pmatrix} z+d \\ 0 \\ -x \end{pmatrix}. \tag{2.13}$$

To find the gradients and curvatures that will be relevant later, we expand this around $(x = 0, z = z_0 + d)$ to 2nd order in $\alpha = \frac{z-z_0}{z_0}$ and $\beta = \frac{x}{z_0}$. This yields

$$B_x = \frac{\mu_0 I}{2\pi z_0}\left[1 - \alpha + \alpha^2 - \beta^2\right], \tag{2.14}$$

$$B_z = \frac{\mu_0 I}{2\pi z_0}\beta\left[1-2\alpha\right]. \tag{2.15}$$

Long broad wire

In atom chip experiments the conductors often have rectangular cross section (cf. Chap 3). Normally the width w of the wires is significantly larger than the thickness h ($w \gg h$). In most experiments the distance of the trapped atoms to the conductor is of the order of the width of the wire. Under these conditions it is inappropriate to approximate the conductors as being cylindrical. A better approximation is that of the infinitely long, thin broad wire. From integration of Biot-Savart for such a wire centered at ($y = 0, z = 0$) and current flowing in the positive x direction we find:

$$B_y(x,y,z) = -\frac{\mu_0 I}{2\pi w}\left[\arctan\left(\frac{y+w/2}{z}\right) - \arctan\left(\frac{y-w/2}{z}\right)\right], \tag{2.16}$$

$$B_z(x,y,z) = \frac{\mu_0 I}{4\pi w}\ln\left[\frac{(y+w/2)^2+z^2}{(y-w/2)^2+z^2}\right]. \tag{2.17}$$

The field straight above the wire is

$$B_y(0,0,z) = \frac{\mu_0 I}{\pi w}\arctan\left(\frac{w}{2z}\right), \tag{2.18}$$

with a gradient along z of [49]

$$\frac{\partial B_y}{\partial z} = \frac{\mu_0 I}{\pi}\frac{2}{w^2+4z^2}. \tag{2.19}$$

Realistic Z wire

Modelling the central part of the Z wire as an infinitely long broad wire gives accurate expressions for the transverse field and transverse gradient, but is in error when it comes to the longitudinal confinement. To include the longitudinal confinement we have to reduce the length of the central part of the Z and add the two ends extending to plus and minus infinity in the y direction. One way to calculate this is to calculate the field of an infinitely thin Z-shaped wire and integrate the result along a finite width w in the y direction. This yields the magnetic field $\mathbf{B}_\mathrm{Z}$ of a Z wire with a central section along x with length $L = 2a$ and width $w = 2b$ centered at the origin and thin, infinitely long ends.

$$\frac{4\pi}{\mu_0 I}\mathbf{B}_\mathrm{Z}(x,y,z) = \frac{1}{(x+a)^2+z^2}\begin{pmatrix} z \\ 0 \\ -x-a \end{pmatrix} + \frac{1}{(x-a)^2+z^2}\begin{pmatrix} z \\ 0 \\ -x+a \end{pmatrix} + \frac{1}{2b}\left[\mathbf{f}(x+a,y-b,z) - \mathbf{f}(x+a,y+b,z) + \mathbf{f}(x-a,y+b,z) - \mathbf{f}(x-a,y-b,z)\right], \tag{2.20}$$

with the auxiliary vector $\mathbf{f}(x, y, z)$:

$$\mathbf{f}(x,y,z) = \frac{r}{x^2+z^2}\begin{pmatrix} z \\ 0 \\ -x \end{pmatrix} + \arctan\left(\frac{xy}{zr}\right)\begin{pmatrix} 0 \\ 1 \\ 0 \end{pmatrix} + \operatorname{arctanh}\left(\frac{x}{r}\right)\begin{pmatrix} 0 \\ 0 \\ 1 \end{pmatrix}, \quad (2.21)$$

where r is:

$$r = \sqrt{x^2+y^2+z^2}.$$

To describe our complete trapping field we have to add to this the field of the miniwire, Eq. (2.13) at a depth d underneath the chip surface and the uniform field

$$\mathbf{B}_{\text{bias}} = \begin{pmatrix} B_{\text{bias},x} \\ B_{\text{bias},y} \\ 0 \end{pmatrix}, \quad (2.22)$$

produced by external coils.

Equations (2.13), (2.20) and (2.22) yield a very accurate analytical approximation of the magnetic field that can serve as alternative for a full numeric simulation of the trapping field. The most important simplifications in this analytical approach are the thickness of the Z wire that is set to zero and the width of the two ends of the Z wire, that is also taken to be zero. The influence of these simplifications can be neglected in our experiment as the distance between the Z wire and the trapping region is much larger than the thickness of the Z wire and the distance of the trapping region to the ends of the wire is much larger than the widths of these ends.

Although suited to replace numerical simulations, the expression (2.20) is not very useful for manipulation by hand. For this purpose it is better to approximate the magnetic field near the trap center as

$$\mathbf{B}(x,y,z) = \begin{pmatrix} B_{x,0} + C(x^2-z^2) \\ Gz \\ Gy - 2Cxz \end{pmatrix}, \quad (2.23)$$

where the coordinate system has been shifted in the direction of z such that the origin coincides with the magnetic field minimum. The constant C relates to the longitudinal trapping frequency like

$$\omega_{\parallel} = \sqrt{\frac{m_F g_F \mu_B}{m}\frac{d^2 B_x}{dx^2}} = \sqrt{\frac{m_F g_F \mu_B}{m} 2C}, \quad (2.24)$$

while the gradient G, together with the longitudinal field B_x, corresponds to the transverse trapping frequency

$$\omega_{\perp} = \sqrt{\frac{m_F g_F \mu_B}{m}\frac{G}{B_x}}. \quad (2.25)$$

The actual values of the bias field gradient and curvature in Eq. (2.23) depend on the precise geometry and respective currents in the two wires of Fig. 2.1 and the applied bias field. For instance, comparison of (2.23) and (2.14) shows that the contribution of the miniwire to the curvature is $C = -\frac{\mu_0 I}{2\pi(z_0+d)^3}$ while the contribution of the Z wire to C and G follows from Eq. (2.20). G is approximated nicely by Eq. (2.19).

2.3 Radio-frequency dressed potentials

We have described static magnetic potentials in which neutral atoms can be trapped if they are in a low-field seeking state [positive m_F in Eq. (2.1)]. These states have higher energy than the $m_F \leq 0$ states, but as long as the adiabaticity criterion is satisfied the energy separation is large and no transitions to the lower energy states occur at the timescale of experiments. In the following section we look at the influence of a radio-frequency magnetic field with which we couple the spin states. We assume a linear Zeeman effect such that there is only one resonance frequency to couple all states. The atoms are not necessarily lost from the trap due to the induced spin flips. Instead a new effective potential arises in which they can remain trapped.

Figure 2.2 illustrates the principle. Fig. 2.2(a) shows the potential of the 5 Zeeman states of an $F = 2$ atom around the static magnetic field minimum of a waveguide [Eq. (2.12)]. The arrows indicate the position where the rf is resonant with the energy spacing between the levels. Because the Zeeman effect is linear, the position of the resonance is independent of the level. Fig. 2.2(b) shows the resulting potential including the rf. The potential for $\tilde{m} > 0$ has two minima separated by a barrier with finite height, while the $\tilde{m} < 0$ states see a single, shallow potential well.

The resulting effective potential is called rf-dressed potential. The name refers to the dressed atom picture that was developed in the 1960s by Haroche and Cohen-Tanoudji [36, 100]. It gives a full quantum mechanical treatment of an atom in a radiation field, quantizing both the radiation field and the atom. We will show in Sec. 2.3.1 that such a rigorous treatment is not essential in our case. We can also describe the potential by treating the radiation field classically. Still these potentials are referred to here as rf-dressed potentials.

In 2001 Zobay and Garraway proposed the use of rf-dressed potentials in neutral atom trapping and cooling experiments, not for evaporation, but to modulate the trapping potential [101, 102]. They showed that by adding a static and rf magnetic field a new, two-dimensional, trap is created in which neutral atoms can be loaded and trapped. The idea was soon validated in a first experiment [78] that was followed by others [79, 82]. Although rf-dressed potentials are not limited to atom chips, especially in combination with chips they have been very successful in the creation of double-well potentials and matter-wave interferometers and the study of (nearly) 1D systems [72, 103].

Strictly speaking the use of rf-dressed potentials was not new to the field in 2001. The established technique of forced rf evaporation also combines a static and an rf magnetic field but with the goal to remove atoms from a trap. Radio-frequency evaporation was first suggested in 1989 [104] and used in the mid-1990s to achieve BEC [19–21]. Nowadays forced evaporative cooling [43, 105, 106] is the standard method employed in numerous atomic physics experiments to deliver the final increase in phase space density before reaching quantum degeneracy. The difference between rf evaporation and the rf-dressed potentials that we are considering here depends on the dressed state quantum number $\tilde{m}$ which is $-F$ in the usual rf evaporation scheme, while it is $+F$ for the split double-well potential. The quantum

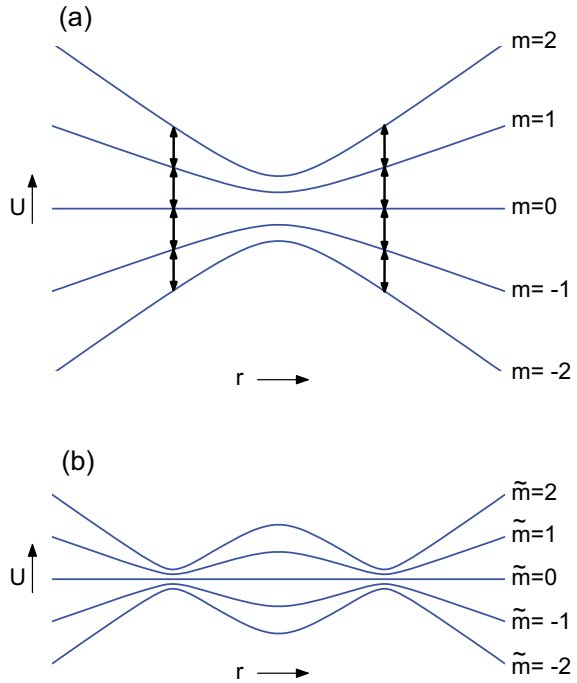

Figure 2.2: Comparison of the bare spin states in a static magnetic trapping potential for an atom with $F = 2$ (a) and the states in an rf-dressed potential (b). The static magnetic field is that of a waveguide [Eq. (2.12) with $r = \sqrt{y^2 + z^2}$]. Plotted is the potential U against the spatial coordinate r. The arrows in (a) indicate the position where the rf is resonant with the energy spacing between the levels.

number in turn is determined in practice by the frequency at which the rf field is switched on.

2.3.1 The rf-dressed potential

Here we present an expression for the rf-dressed potential and give a brief outline of the derivation. The complete derivation for linearly polarized rf is treated in more detail in Appendix A.

The Hamiltonian for a neutral atom with a magnetic moment experiences in a time-dependent magnetic field $\mathbf{B}(t)$ is

$$\hat{H} = -\hat{\boldsymbol{\mu}} \cdot \mathbf{B}(t), \tag{2.26}$$

which is the same as in the static case apart from the time dependence of the magnetic field. The total $\mathbf{B}(\mathrm{t})$ field can be divided in a static part $\mathbf{B}_\mathrm{s}$ and an oscillatory part $\mathbf{B}_\mathrm{rf}(t)$.

Classically, in the absence of an oscillatory field, the magnetic moment will precess around the static field with an angular frequency given exactly by the Larmor

frequency Eq. (2.3), which also gives the spacing of the quantum-mechanical energy levels. The part of the time-dependent field $\mathbf{B}_{\mathrm{rf}}$ that is perpendicular to the static magnetic field can now be decomposed into two rotating components: one rotating with the precessing atom, and another component rotating against the direction of precession. A key step that can now be made is the so-called rotating-wave approximation (RWA) [108]. It consists of only taking into account the co-rotating component. This approximation is particularly good when the oscillation frequency of the rf field is close to the Larmor frequency. In that case, the co-rotating component will appear as a (nearly) static term in the frame rotating with the precessing atom. Physically, in the rotating frame the atom will actually see a reduced static longitudinal field together with the slowly-varying co-rotating component mentioned above. The magnetic moment will now precess around the (nearly) static field in this frame. Other (non-co-rotating) terms will oscillate so rapidly in this rotating frame that their effect averages out as long as these non-RWA terms are weak enough.

In short, if we take a linearly polarized, sinusoidally time-dependent rf field with frequency ω_{rf}, and strength b_{rf} perpendicular to $\mathbf{B}_{\mathrm{s}}$, the effective static magnetic field in a frame rotating at a frequency ω_{rf} is

$$\tilde{\mathbf{B}} = \left(B_{\mathrm{s}} - \frac{\hbar\omega_{\mathrm{rf}}}{|g_F \mu_B|} \right) \mathbf{e}_z + \frac{1}{2} b_{\mathrm{rf}} \mathbf{e}_x. \tag{2.27}$$

The factor of two lowering in the effect of b_{rf} is directly related to the fact that only the co-rotating part of the linear rf field contributes to the effective magnetic field.

Thus, the new potential can be expressed as

$$U = \tilde{m}\hbar\sqrt{\Delta^2 + \Omega^2}, \tag{2.28}$$

with $\tilde{m} = -F, \ldots, F$, where Δ^2 is called the resonance term with Δ the detuning of the rf frequency with respect to the Larmor frequency

$$\Delta = \omega_{\mathrm{rf}} - \omega_L = \omega_{\mathrm{rf}} - \frac{|g_F \mu_B|}{\hbar} |\mathbf{B}|. \tag{2.29}$$

The other term, Ω^2, is referred to as the coupling term. The position-dependent Rabi frequency is given by the circularly polarized rf-field component referenced to the local direction of the static magnetic field:

$$\Omega = \frac{|g_F \mu_B|}{\hbar} \frac{|\mathbf{b}_{\mathrm{rf}} \times \mathbf{B}|}{2|\mathbf{B}|}. \tag{2.30}$$

In general the RWA fails for $\Delta, \Omega \gtrsim \omega_L/3$. Above these values non-RWA, also called beyond-RWA, contributions must be taken into account to accurately describe the potential. In experiments characterizing the potential with rf spectroscopy the non-RWA contributions show up as a shift of resonances and the appearance of new resonances [109, 110].

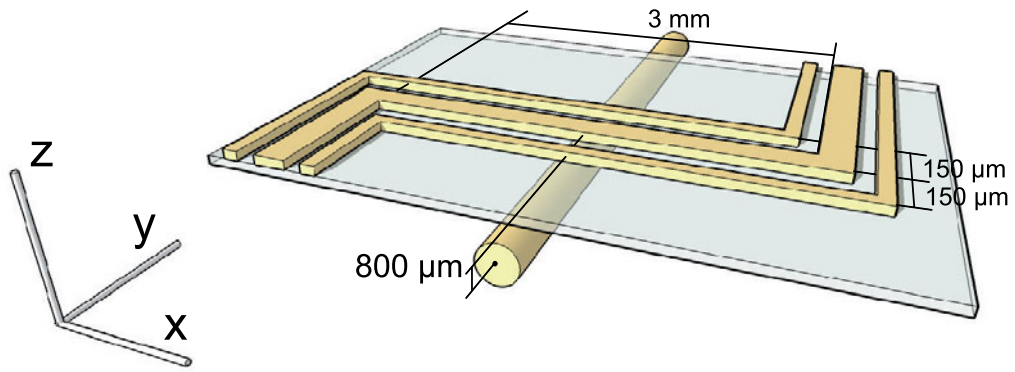

Figure 2.3: Sketch of both wires producing the static magnetic trap and the rf wires. The rf wires are positioned symmetrically with respect to the central Z wire. See Fig. 2.1 for the geometry without the rf wires.

2.3.2 RF magnetic field

We generate the radio-frequency field which we need to create radio-frequency potentials using two on-chip wires. The geometry is shown in Fig. 2.3. We use two wires, positioned symmetrically with respect to the central Z wire producing the static magnetic trap. The rf wires also have an overall Z shape. The close proximity of these wires to the trapped atoms ($\sim$200 μm) allows us to achieve large field strength ($\sim$1 G) with minimal effort (10–100 mA). To create such an rf field with a coil inside the vacuum system (or worse, outside the vacuum system) would require much more effort.

A consequence of the use of wires that are close to the atoms instead of larger coils is the existence of field gradients that we have to deal with. These gradients complicate our experiments because we have to compensate for the differences caused by different rf field strengths at various heights of the trap above the wire. On the other hand the rf field gradient also helps us since it can be used to compensate the effect of gravity on the trapped atoms. The effect of gravity and its compensation is treated in more detail in Sec. 5.4.3.

The use of two separate chip wires to produce the rf field give us the possibility to vary the rf polarization. By tuning the rf amplitude ratio in the two wires and setting the phase difference to either 0 rad or π rad we can produce linearly polarized rf in any direction in the y-z plane (note that the central parts of the rf wires run in the x direction, so that $\mathbf{B}_{\mathrm{rf}}$ is predominantly in the y-z plane around the center of the trap). The direction of the linear polarization we denote by θ, the polarization angle in the y-z plane with respect to the y axis, such that:

$$\mathbf{B}_{\mathrm{rf}} = \begin{pmatrix} 0 \\ b_{\mathrm{rf}} \cos\theta \\ b_{\mathrm{rf}} \sin\theta \end{pmatrix}, \tag{2.31}$$

where b_{rf} is the amplitude (> 0) of the rf magnetic field $\mathbf{B}_{\mathrm{rf}}$. The Rabi frequency

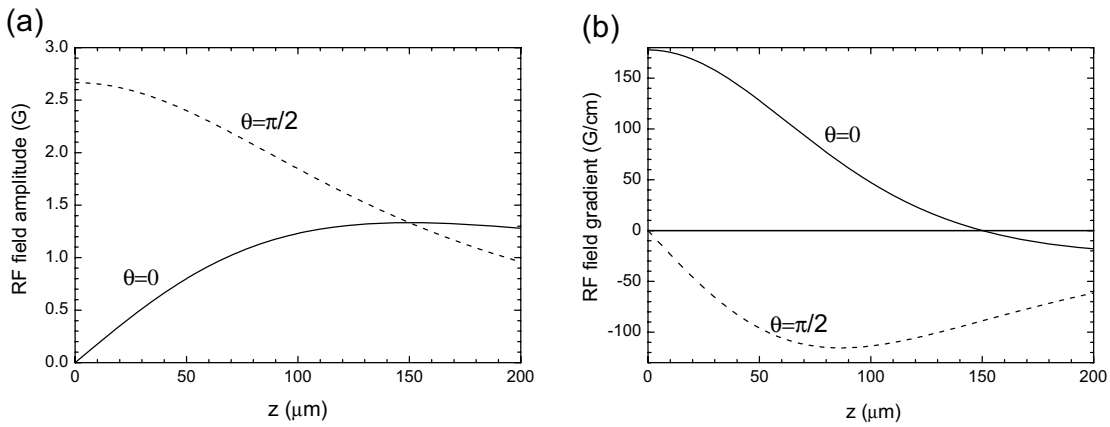

Figure 2.4: RF dressing field strength (a) and RF dressing field gradient (b) as a function of z coordinate. The fields were calculated using Eq. (2.33) for a sinusoidal current with an amplitude of 100 mA in both wires and y_{rf}=150 μm. The solid line corresponds to the case that both currents have equal phase and the direction of the rf field is in the y direction (θ=0). The dashed line corresponds to currents in counter-phase and the rf field in the z direction (θ=$\pi/2$).

now becomes

$$\Omega = \frac{|g_F \mu_B|}{\hbar} \frac{b_{\mathrm{rf}} \sqrt{B_x^2 + (B_y \sin\theta - B_z \cos\theta)^2}}{2|\mathbf{B}|}, \tag{2.32}$$

where B_x, B_y and B_z are the components of the static magnetic field.

To obtain an expression for $\mathbf{B}_{\mathrm{rf}}$ in the trapping region in terms of the rf wire currents I_1 and I_2 and the wire spacing $|y_1| = |y_2| = y_{\mathrm{rf}}$, we consider only the central section of the two rf wires and model them as infinitely long, thin, straight wires. This approximation is reasonable since the distance between these wires and the atoms is much larger than the width of the wires, while on the other hand the distance is small compared to the length of the central section of the Z. The phase difference ϕ between rf currents is included by taking I_1 and I_2 with equal sign for $\phi = 0$ rad and with opposite sign for $\phi = \pi$ rad. We arrive at

$$\mathbf{b}_{\mathrm{rf}}(0,0,z) = -\frac{\mu_0}{2\pi\left(y_{\mathrm{rf}}^2 + z^2\right)} \begin{pmatrix} 0 \\ z(I_1 + I_2) \\ y_{\mathrm{rf}}(I_1 - I_2) \end{pmatrix}, \tag{2.33}$$

by using Eq. (2.9) for each wire and taking the superposition of the two fields. We see that we can indeed set any value of θ by tuning the rf current ratio.

Figure 2.4 shows the rf magnetic field strength and gradient for realistic numbers ($|I_1| = |I_2| = 100$ mA, $y_{\mathrm{rf}} = 150$ μm). Notice that the rf magnetic field gradient in the direction of z is positive for θ=0 and negative for θ=$\pi/2$.

It is also possible to apply a phase difference of $\varphi = \pi/2$ or $\varphi = 3\pi/2$ to the rf currents. In that case the field will have elliptical polarization because in general the two field components of the two wires are not perpendicular. Only at one specific height, $z = y_{\mathrm{rf}}$, the fields are perpendicular and the polarization is circular for equal

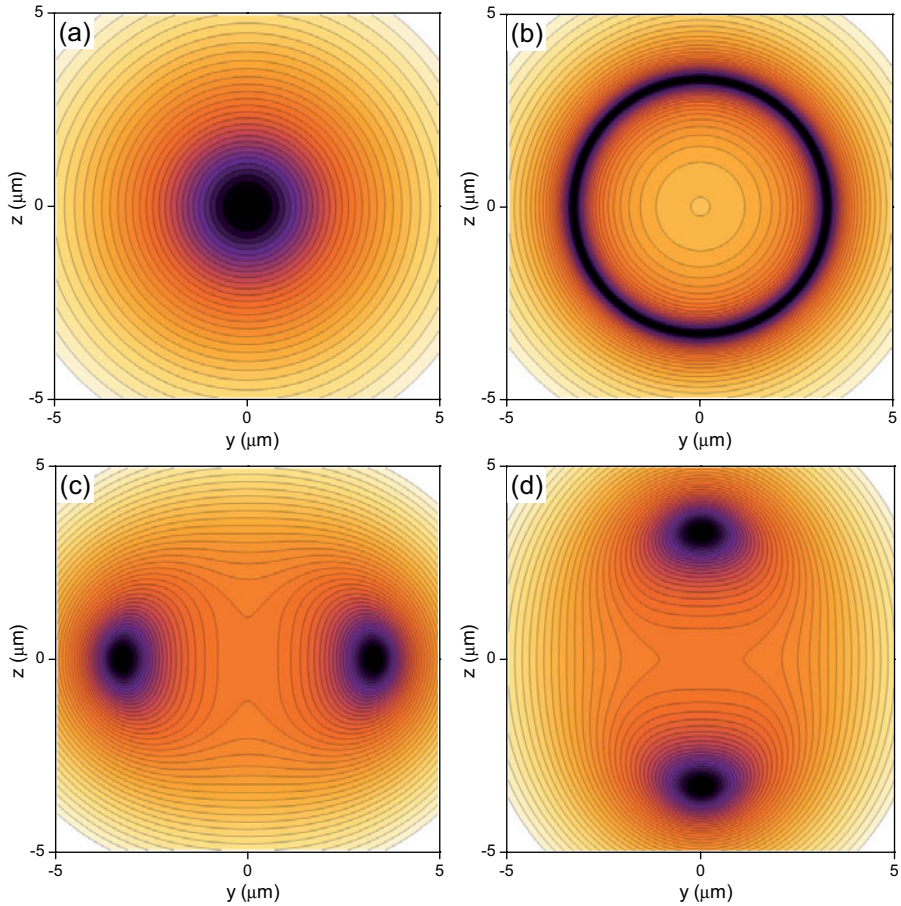

Figure 2.5: Cross-sections of 4 (rf-dressed) potentials at $x = 0$. Lighter color denotes higher potential; atoms are trapped in the dark-colored potential minima. The 4 plots are for identical static magnetic fields. The rf-dressing field is different in the 4 plots. In (a) the rf-dressing field is absent and we are left with the bare magnetic potential. In (b) the rf field polarization is circular, rotating in the y-z plane. The potential has the shape of a Mexican hat. In (c) the rf field vector is oriented vertically (direction of z) and the potential minimum splits in the direction of y. In (d) the splitting is in the direction of z, while the rf field vector is along y. See the text for more details.

currents, $I_1 = I_2$. In most of the experiments described in this thesis we limited ourself to linear polarization.

2.3.3 Character of the rf-dressed potential

RF-dressed fields can be used to modulate the trapping potential in ways that are not allowed for static magnetic potentials because of Maxwell's equations. Before looking in detail at one specific rf-dressed potential, the double-well, we will first look at the general shape of these potentials.

Figure 2.5 shows cross-sections of 4 different potentials in the y-z plane at $x = 0$.

Because the x dependence of the static magnetic field is generally weak and because the rf field is only weakly dependent of x the most interesting features of these potentials can best be observed in the y-z-plane.

For low rf frequency ($\omega \ll \omega_L$), the detuning is large and the resonance term in Eq. (2.28) dominates over the coupling term. In this case the rf dressed potential looks just like the bare potential [Fig. 2.5(a)]. For increasing rf frequency, the resonance term first decreases to zero ($\omega_{\mathrm{rf}} = \omega_L$) and then starts to grow again. But while the resonance term in the center is growing again, parts outside the center with a larger static field amplitude are at resonance. The resonance term defines a resonance surface that is an ellipsoid in three dimensions and to first approximation a circle in the y-z plane. The coupling term in Eq. (2.28) further structures the potential minimum at the resonance surface. Note that in the static field minimum the rf field vector is perpendicular to the static field aligned along x and the coupling term is maximum. Moving from the center outward, the static field vector turns away from x and also has components in the y-z plane. Moving from the center outward along z, the field has a growing B_y and the field vector rotates toward y [see Eq. (2.11) or Eq. (2.23)]. On the other hand moving from the center in the direction of y the static field has an increasing B_z and the field vector turns into the direction of z. Now assume a linearly polarized rf field with field vectors along z. Moving from the center in the direction of z, the static field vector rotates but always stay perpendicular to the rf field. The magnitude of the coupling term in Eq. (2.28) is constant. Moving in the direction of y something else happens. There the static field vector aligns in the direction of the rf field vector reducing the coupling term. So the resonance term makes that the minima are on a ring and the coupling term makes that, for this particular rf field, they are in the plane $z = 0$. This is the situation of Fig. 2.5(c). A rf field directed along y produces minima at $y = 0$ [Fig. 2.5(d)].

Fig. 2.5(b) shows the potential for a circularly polarized rf field. In this case the rf field vector is rotating in the y-z plane and the angle of the static field with respect to the rotating field is the same everywhere along the resonant circle. The contribution of the coupling term to the potential is equal everywhere along the circular resonance surface. The potential minimum thus remains circular resulting in a Mexican hat potential.

In the x direction the potential varies only slowly due to the relatively weak longitudinal confinement. As a consequence the resonance circle in the y-z plane slowly gets smaller when moving along x away from the trap center. At some distance from the center the ring merges in one point, closing the 3D ellipsoid that describes the resonant surface.

2.4 Electrostatic manipulation

In the preceding sections we have only discussed potentials formed by magnetic fields. Electrostatic fields can also be used to trap and manipulate neutral atoms [50, 98]. For the Rb atom, with its single unpaired electron, the electric polarizability α is

a scalar. The polarizability of ^{87}Rb atoms in the $5s\,^2S_{1/2}$ state is 5.3×10^{-39} Cm^2/V [111]. The interaction energy of the induced dipole $\mathbf{d}$ and the electric field $\mathbf{E}$ is:

$$U_{\mathrm{el}}(\mathbf{r}) = -\mathbf{d} \cdot \mathbf{E} = -\frac{1}{2}\alpha E^2(\mathbf{r}). \tag{2.34}$$

The electrostatic interaction can be used to enhance the functionality of magnetic atom chips for instance with beam splitters or a 'motor' to transport atoms along a magnetic guide [56].

Given the typical dimensions of the wires on the atom chip and the distance of the trapped atoms to the surface (both tens of μm) voltages of ~ 200 V are needed to make the strength of the electrostatic and magnetic interaction comparable for ^{87}Rb in the $F = 2$ state. This is also roughly the value of the voltages used in [56].

2.5 Properties of trapped ultracold gases

2.5.1 In-trap longitudinal density distributions

The past sections have dealt with the precise details of the trapping potential $V(\mathbf{r})$. This trapping potential determines to a large extent the density distribution of the atoms in a (quantum) gas. The two simplest cases that are usually considered for a Bose gas are (i) a "classical" gas, where effects of quantum degeneracy can be ignored, and (ii) a "condensate" near zero temperature, where the effects of a finite (non-zero) temperature can be ignored.

In the elongated trapping geometry that is typical in atom traps these two regimes are separated not only by the phase transition associated with Bose-Einstein condensation, but also by various cross-overs, for example going from 3D to 1D. An extensive overview of the cross-overs that are typically encountered for a Bose gas on an atom chip can be found elsewhere (Ch. 2 of [88] and references therein). Here, we limit ourselves to two cases that will be relevant in the subsequent chapters, and discuss how one can extract the potential shape from the observed longitudinal density distribution in both cases.

First, for a "classical" gas, when temperature is sufficiently high and density sufficiently low that effects of degeneracy and interactions are negligible, the density distribution is given by Boltzmann's law

$$n(\mathbf{r}) = n_0 \exp\left(-V(\mathbf{r})/k_{\mathrm{B}}T\right), \tag{2.35}$$

where k_B is Boltzmann's constant and T is the temperature. In Ch. 3 we will want to infer the longitudinal potential from the observed density distribution. If the 3D potential $V(\mathbf{r})$ can be written as a sum over a radial potential $V_{\mathrm{rad}}(y, z)$ and a longitudinal potential $V_{\mathrm{l}}(x)$, this can be done by radially integrating over the above density distribution and inverting the result, yielding

$$V_{\mathrm{l}}(x) = -k_{\mathrm{B}}T \ln\left[n_{\mathrm{l}}(x)/n_{\mathrm{l},0}\right], \tag{2.36}$$

with $n_{\mathrm{l}}(x)$ the measured longitudinal linear density.

Second, in the opposite extreme of near-zero temperatures, the physics of the resulting condensate is dominated by the interaction energy, which in turn determines the chemical potential μ. In 3D, for a weakly interacting gas this is summarized by the simple relation

$$\mu = g n_0, \tag{2.37}$$

with g the 3D coupling constant,

$$g = \frac{4\pi\hbar^2 a}{m}, \tag{2.38}$$

with a the scattering length (5.24 nm for ^{87}Rb in the $F = 2$, $m_F = 2$ state). In 1D a similar equation holds near zero temperature, with an effective 1D coupling constant [112].

A simple analytical description for the density distribution found by Gerbier [113] that works well throughout the 3D-1D crossover for sufficiently low temperatures will be useful in the following Chapters. Assuming harmonic confinement in the radial directions with a frequency $\omega_\perp$, he found

$$\mu = \hbar\omega_\perp \left(\sqrt{1 + 4a n_{\mathrm{l}}} - 1\right), \tag{2.39}$$

with n_{l} the linear density along the longitudinal direction. The latter result can also be used to infer the longitudinal potential from the measured linear density, by using a local-density approximation

$$\mu(x) + V(x) = \mu, \tag{2.40}$$

where $\mu(x)$ is the local chemical potential, referenced to the local potential energy $V(x)$ and the global chemical potential μ. This yields

$$V(x) = -\hbar\omega_\perp \left(\sqrt{1 + 4a n_{\mathrm{l}}(x)} - 1\right). \tag{2.41}$$